Focus Section: Statistical Seismology

Testing Rate-and-State Predictions of Aftershock Decay with Distance

Morgan T. Page*[1], Nicholas J. van der Elst[1], and Sebastian Hainzl[2,3]

Abstract

We analyze aftershocks of the 2019 *M* 7.1 Ridgecrest mainshock and isolated *M* 5–6 mainshocks in southern California to test predictions made by the rate-and-state friction model of Dieterich (1994). Rate-and-state friction predicts that the seismicity rate after a stress step follows Omori decay, where the Omori *c*-value, which is the saturation in aftershock rate observed at small times, is larger for smaller stress steps. Put in the context of an aftershock sequence, this predicts that the Omori *c*-value will be systematically larger at greater distances from the mainshock. To our knowledge, this predicted effect has not been observed. In part this may be because the Omori *c*-value is difficult to measure because it often reflects short-term catalog incompleteness rather than a true saturation in aftershock rate.

We explore the dependence of the Omori *c*-value on the distance to the mainshock by applying the "*a*-positive" method (van der Elst and Page, 2023). This method is insensitive to short-term aftershock incompleteness and allows resolution of the true aftershock rate deep into the mainshock coda. For aftershocks of the Ridgecrest mainshock and stacked *M* 5–6 mainshocks, we observe systematic differences in early aftershock rates, relative to mainshock distance, consistent with the predictions of rate-and-state friction. Furthermore, for the larger Ridgecrest dataset, we observe that aftershocks nearer to the mainshock start earlier, and we resolve a flattening of the Omori curve consistent with a larger Omori *c*-value for the farthest aftershocks, as predicted by Dieterich (1994).

Cite this article as Page, M. T., N. J. van der Elst, and S. Hainzl (2024). Testing Rate-and-State Predictions of Aftershock Decay with Distance, *Seismol. Res. Lett.* **XX**, 1–11, doi: 10.1785/0220240179.

Supplemental Material

Introduction

In his classic article, Dieterich (1994) shows that rate-and-state friction can reproduce the Omori–Utsu (Omori, 1895; Utsu, 1961) law of aftershock decay. In particular, following an instantaneous stress step $\Delta\tau$, for the case with no stressing rate following the step (that is, zero background rate), the rate of aftershocks as a function of time t is given by

$$R(t) = \frac{r}{e^{\frac{-\Delta\tau}{A\sigma}} + t\dot{\tau}_r/A\sigma}, \tag{1}$$

in which r is the reference seismicity rate (the rate prior to the stress step); A is a rate-and-state parameter controlling the size of the instantaneous "direct" effect; σ is effective normal stress; and $\dot{\tau}_r$ is the stressing rate prior to the stress step. This is equivalent to the Omori–Utsu law, which states that the rate of aftershocks as a function of time t following a mainshock decays as $(t + c)^{-p}$, for the case in which $p = 1$ (see Fig. 1). The c-value in the Omori–Utsu law prevents the rate from diverging at $t = 0$ and results in a saturation in rate at short times (see Fig. 1).

In nature, Omori decay is often observed with $p \neq 1$. The rate-and-state model predicts that the p-value is lowered by stress-step heterogeneity; that is, a population of aftershocks in an area where $\Delta\tau$ is variable and will have $p < 1$ (Dieterich, 1994). Note that this depression of the p-value is a consequence of c-value variability.

In addition to Omori aftershock rate decay, the rate-and-state model predicts seismic quiescence in regions of stress decrease (stress shadows), which has been observed at later times in the aftershock sequence (Harris and Simpson, 1998; Mallman and Parsons, 2008), following an initial burst of presumably dynamically triggered earthquakes in the shadow region (Mallman and Parsons, 2008; Hardebeck and Harris, 2022). Equation (1) also predicts that the aftershock rate is proportional to background rate (the steady-state rate prior to the stress step), which has been observed in the spatial

1. U.S. Geological Survey, Pasadena, California, U.S.A., https://orcid.org/0000-0001-9321-2990 (MTP); https://orcid.org/0000-0002-3812-1153 (NJE); 2. GFZ German Research Centre for Geosciences, Potsdam, Germany, https://orcid.org/0000-0002-2875-0933 (SH); 3. Institute of Geosciences, University of Potsdam, Potsdam, Germany

*Corresponding author: mpage@usgs.gov

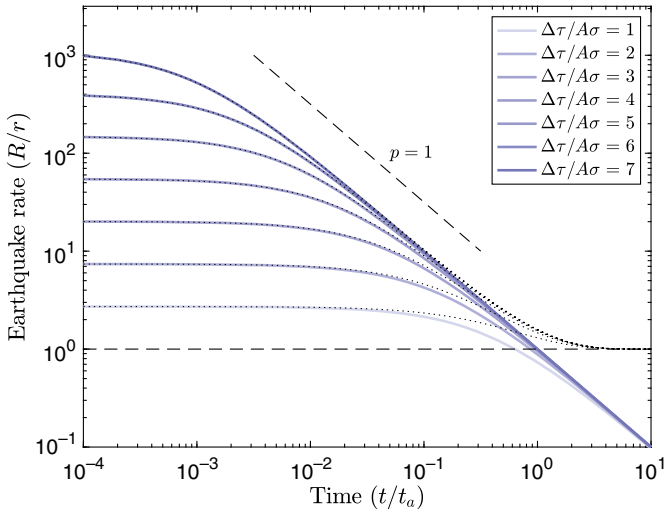

Figure 1. Rate-and-state prediction for seismicity rate following a stress step, adapted from Dieterich (1994). The blue curves show the prediction from equation (1), which assumes no background rate; dotted curves show predictions adding in a background rate of 1 (horizontal dashed line). The color version of this figure is available only in the electronic edition.

distributions of individual mainshock sequences, when stacked (Page and van der Elst, 2022).

The key prediction we test here, evident in equation (1), is that the Omori c-value increases as the stress step decreases (see Fig. 1). In the context of an aftershock sequence, this implies that aftershocks farther away from the mainshock, which, on average, experience a smaller stress step than aftershocks close to the mainshock, will follow an Omori trend with a higher c-value. Thus, for aftershocks farther from the mainshock, there should be a longer delay between the mainshock time and the onset of a power-law decay in aftershock rate. In this article, we look for this effect following the M 7.1 Ridgecrest mainshock and other moderate-size mainshocks in southern California.

Assumptions needed to produce Omori's law under rate-and-state friction

A few key assumptions are necessary in order for a population of rate-and-state faults to recover Omori's law (Dieterich, 1994). The most important of these assumptions is that the population of receivers is uniformly distributed throughout the seismic cycle with respect to failure time, that is, that the background rate is constant in the absence of a stress step. This assumption is crucial for obtaining a constant rate (plateau) at early times prior to c. Different temporal behavior will be obtained for aftershocks triggered from a different distribution.

The second major assumption of the Dieterich constitutive law is referred to as the no-healing limit (Dieterich, 1994), which assumes that the fault is always left closer to failure after a stress perturbation, and which allows the state variable (the velocity-independent component of fault strength) to be simplified out of the equations. This is considered consistent with the "aging" law used to describe the evolution of fault state in the laboratory, but not with the "slip" law, in which faults can initially weaken or strengthen depending on the magnitude of the velocity increase and where the fault is within its cycle (Gomberg *et al.*, 2000; van der Elst and Savage, 2015). Although the "slip" law is preferred to explain many modern lab experiments, in particular those that involve a large instantaneous stress step (Bhattacharya *et al.*, 2017), it fails to reproduce Omori's law on uniformly distributed receivers. This disagreement with Omori's law has been used as evidence that the "slip" law is not relevant for rate-and-state triggering in nature (Gomberg *et al.*, 2000; Heimisson and Segall, 2018).

Another assumption is that receiver faults are characterized by a uniform strength parameter $A\sigma$. If this assumption is relaxed, then the distribution of failure times will again be altered, with ramifications for what can be estimated or constrained by observation. Finally, any observation of Omori's law in nature will involve a distribution of faults subjected to a distribution of stress changes. This again changes the shape of the temporal decay. For example, a homogeneous distribution of receivers with distance gives values of p <1 (Dieterich, 1994). In the next section, we examine the effect of some of these assumptions, using a toy model.

Insights from block-slider modeling

Which of the features and predictions of rate-and-state triggering should be observable in real catalogs? We investigate this using numerical modeling of a toy rate-and-state frictional slider. The slider is subjected to stress steps to produce clock-advanced "aftershocks." The dynamical equations for the slider are described in Rice and Ruina (1983); the specific implementation is described in van der Elst and Savage (2015), along with the parameters used and details on setting the initial state of the system. Only the qualitative features of the modeling are important for this introduction, and the details of the numerical modeling will not be reproduced here. Parameters are chosen to produce regular stick-slip sliding in the absence of a perturbation, with $A\sigma = 0.1$ MPa and an aftershock duration $t_a = A\sigma/\dot{\tau}_r$ that is about 4% of the seismic cycle, defined as the time between slip events under constant loading. The nondimensionalized behavior of the slider does not depend strongly on the interface frictional parameters, as long as the parameters support stick-slip sliding (table 2 of van der Elst and Savage, 2015). This accounts for the success of the Dieterich constitutive model, which depends only on $A\sigma$ and t_a. For full reproducibility, the specific frictional parameters (defined in van der Elst and Savage, 2015) are A = 0.02, B = 0.0365, and $d_c = 1$.

Each of a population of 100 sliders is loaded at a constant stressing rate and subjected to an instantaneous stress step at

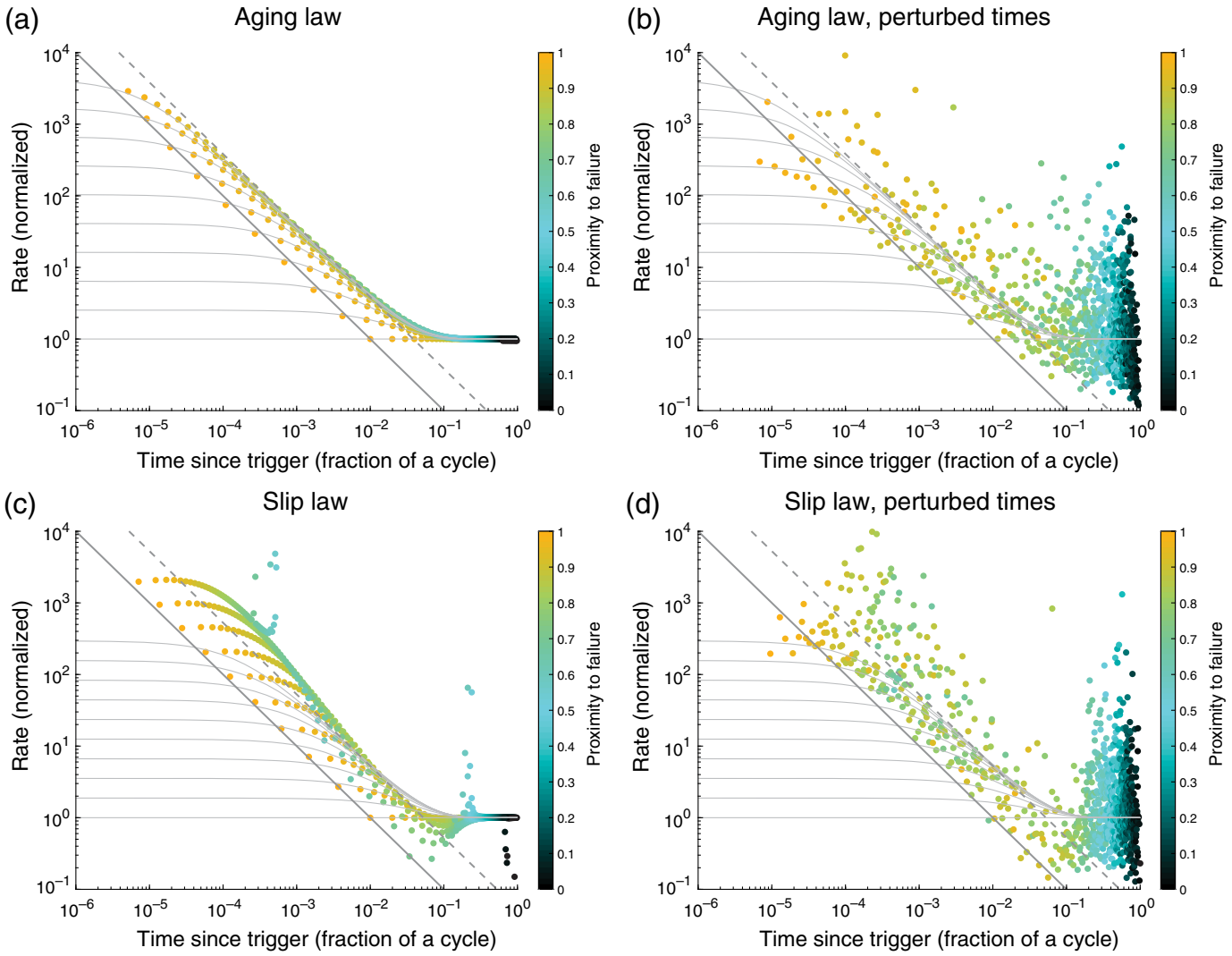

Figure 2. Numerical simulations of a rate-and-state slider block and the effects of stacking populations subjected to different stress. (a) Results for the aging law. Interevent times are computed for stress steps varying from 0% to 30% of the cycle stress drop on sets of receiver faults distributed uniformly with respect to the seismic cycle. The dashed diagonal line shows the expected relationship between R_0 and c (equations 2 and 3). The solid diagonal line shows the expected time to the first aftershock based on equation (4), assuming the next background earthquake had 1% of its cycle remaining. Thin lines refer to the theoretical decay of the rate-and-state seismicity model. (b) Stacked sequence of events from panel (a) with times perturbed by 1% to simulate a small amount of natural variability. (c,d) The same as panels (a) and (b), respectively, but for simulations using the slip law. The stacking obscures much of the difference between the state evolution laws (panels b and d). The color version of this figure is available only in the electronic edition.

selected times within the cycle, and allowed to evolve (Fig. S1, available in the supplemental material to this article). This is done for ten stress levels distributed uniformly between 0% and 30% of the cycle stress drop (the range is limited by numerical tractability). The response of the slider is allowed to evolve until "failure," defined by the state variable falling below 1% of its peak value. Rates are determined between successive events within the population and plotted at the time of the first event in the pair to highlight the onset time, in Figure 2a.

The main complication in extracting physical information from Omori's law is due to stacking events with different triggering stress (Fig. 2). Plotting a single Omori's law for an entire sequence combines regions subjected to very different stress steps. In the ideal case, this leads to an apparent shift in the p-value due to the superposition of curves with differing c-values (Dieterich, 1994). In our numerical simulations, even the basic form of the aftershock decay is obscured by stacking, and much of the difference between the aging and slip laws for state evolution is obscured (Fig. 2). This reminds us that inferences about precise triggering mechanisms remain somewhat nonunique in this analysis and points to the importance of isolating aftershock populations with similar conditions subject to similar stress changes.

One prediction of the rate-and-state model that remains robust to variations in $A\sigma$, stress step, and state-evolution

law is the fundamental scaling between the initial triggered rate increase R_0 and the c-value. These two parameters are expressions of the same exponential dependence between slip rate and stress, and they are inversely related (equations 2 and 3), which provides us with a consistency test on our estimates of c and R_0:

$$c = t_a e^{-\frac{\Delta\tau}{A\sigma}}, \tag{2}$$

$$R_0 = r e^{\frac{\Delta\tau}{A\sigma}}. \tag{3}$$

If the rate of aftershocks R_0 is flat prior to time c, such that the time to the nth aftershock $t^{(n)} \propto R_0^{-1}$, then equations (2) and (3) combine to give additional predictions (equation 4). First, the rate at the time of nth earthquake prior to c also follows Omori's law with $p = 1$ regardless of state-evolution law, as shown by the solid diagonal lines in the panels of Figure 2. Second, any aftershocks prior to time c, without the stress step, would have occurred as background earthquakes prior to time t_a (equation 4). Thus, the plateau in Omori's law consists of the earthquakes that would have otherwise been background earthquakes during the aftershock duration,

$$\frac{t^{(n)}}{t_{bg}^{(n)}} = \frac{c}{t_a}. \tag{4}$$

This has some interesting physical implications. The "aftershock duration" t_a in Dieterich (1994) is known in other literature as the "nucleation timescale" (Dieterich, 1992; Beeler and Lockner, 2003) because it also characterizes the duration over which the fault weakens and accelerates to failure at the end of its cycle under constant loading conditions. This means that any aftershocks appearing in the plateau prior to c were already self-nucleating (Heimisson and Segall, 2018); we may not expect to see such earthquakes in nature if aftershock faults are initially somewhat stronger or farther from failure than the more mature mainshock fault.

In this article, we attempt to resolve the Omori c-value by looking at aftershock decay rates at different distances from the mainshock fault. In this way, we hope to isolate populations of faults exposed to a similar stress change, motivated by our experience with the toy model. Because the static stress change decays with distance from the mainshock, c-values should be systematically higher at greater distances from the fault, with an inverse relationship to the initial rate. To our knowledge, this predicted relation between Omori c-value and aftershock distance has not been observed, likely because the true Omori c-value is difficult to resolve given that the detection of smaller events is significantly degraded in the immediate aftermath of a large earthquake. This effect, termed short-term aftershock incompleteness (STAI) (Kagan, 2004), artificially inflates estimated c-values.

To mitigate the effect of STAI, in this article we use the a-positive method (van der Elst and Page, 2023), which provides reliable estimates of the earthquake rate even when the completeness level of the catalog is rapidly changing. In previous work, van der Elst and Page (2023) demonstrated that all aftershocks of Ridgecrest, taken together, do not show a plateau at early times, and that conventional estimates of finite c-values are due to STAI rather than a true saturation of aftershock rate. There is still a question as to whether the true c-value is finite or zero (or, perhaps, as Kagan and Houston, 2005 argued, negative!). In this article, we analyze aftershock rates as a function of distance to determine if a finite c-value is resolvable at any distance, and if it follows the rate-and-state prediction.

The *a*-Positive Method

The a-positive method (van der Elst and Page, 2023) uses interevent times for event pairs where the second earthquake is larger than the first (larger by a user-selected threshold δM_c), to avoid event pairs where a prior larger event prevents detection of a smaller earthquake. Interevent times, relative to an arbitrary reference magnitude M_{ref}, for these complete pairs are given by

$$\tau_i = dt_i 10^{-b^+(M_i+\delta M_c - M_{\mathrm{ref}})}, \tag{5}$$

in which M_i is the magnitude of the first event in the pair; dt_i is the raw interevent time; and b^+ is the Gutenberg–Richter b-value estimated using the b-positive method (van der Elst, 2021). A rate measurement is thus obtained for each event pair, given by $1/\tau_i$.

Note that it is not necessary to choose a completeness magnitude with the a-positive method. Rather, provided that catalog incompleteness is improving with time, as would be the case with network improvements or in a decaying aftershock sequence, we can use all the recorded events in the catalog. The a-positive pair selection rules give confidence that the catalog will be complete at the magnitude level $M_i + \delta M_c$ over the time period of the earthquake pair. The only tunable parameter in the method is δM_c, which, provided it is large enough, can virtually guarantee that given the first event of the pair, the second event of the pair will be detected. In practice, δM_c should be chosen based on the width of the detection function, which has a gradual rather than step-like cutoff in magnitude (e.g., Ringdal, 1976).

The a-positive method thus allows us to take full advantage of more of the events in modern, high-resolution catalogs, even though parts of these catalogs are quite incomplete (Herrmann and Marzocchi, 2020). As shown in van der Elst and Page (2023), this method gives us more sensitivity in the early parts of an aftershock sequence, when the seismic network is saturated and the completeness is poor, to better resolve aftershock rates within the mainshock coda. Here, we apply the a-positive method to different spatial areas of aftershock zones to discern differences in early aftershock rates.

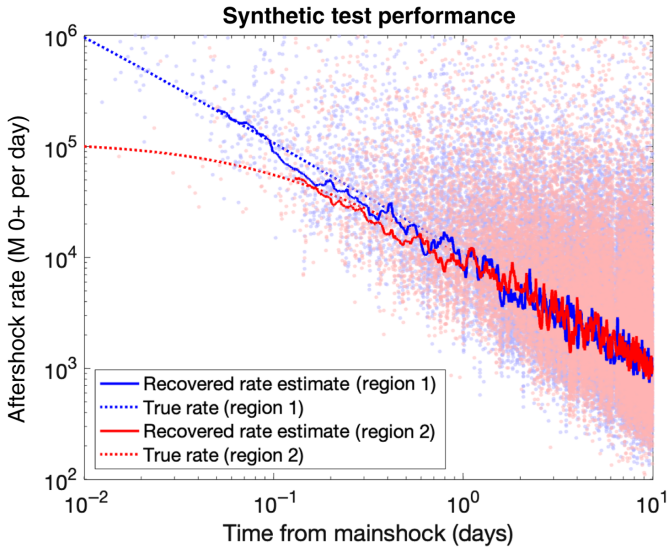

Figure 3. Synthetic test of Omori's law recovery for adjacent regions with different *c*-values. Transparent circles show individual rate estimates for region 1 (blue) and region 2 (red) made using the *a*-positive method. The solid lines show smoothed rate estimates; these compare favorably to the dotted curves, which show the true seismicity rates for each region. The color version of this figure is available only in the electronic edition.

We demonstrate that the *a*-positive method correctly recovers the seismicity rate with a synthetic test. We generate a synthetic seismicity catalog, with magnitudes drawn from the Gutenberg–Richter distribution (Gutenberg and Richter, 1944). In each region, earthquake rates follow Omori decay with $p = 1$, but with different *c*-values. Regions 1 and 2 have *c*-values of 0.001 and 0.1 days, respectively. Transient incompleteness is added that improves linearly in log-time, much as it would, on average, during a real aftershock sequence (Helmstetter *et al.*, 2006). For a given event time, we use the maximum incompleteness from all prior earthquakes; in this way, large aftershocks can temporarily increase the magnitude of completeness. Furthermore, we add noise to the magnitude of completeness so that, at a given time, the probability of detection with magnitude follows a cumulative Gaussian distribution, as has been observed in real seismic sequences, following Ringdal (1976). The result is a synthetic catalog that matches both the mean detected magnitude and its variance, in time, of the catalog that we use in our analysis of the Ridgecrest sequence.

In our synthetic test, events in one region can shadow detection of another. Applying the *a*-positive method in each region independently could lead to underpredictions of rate for this reason if δM_c is too small. For our synthetic test, we find that $\delta M_c = 0.8$ is sufficiently high to recover the true seismicity rates. Results are shown in Figure 3. The recovered rate estimates closely recover the seismicity rates for each region, despite the rapidly changing magnitude of completeness.

Note that part of the signal we observe in our synthetic test is the later onset time for the first detected aftershocks (and first smoothed aftershock rates) for the population with a larger Omori *c*-value. This is consistent with equation (4) and is a consequence of the integrated rates being significantly lower at early times when the *c*-value is larger.

Ridgecrest Sequence Data and Results

We first investigate the temporal decay in aftershocks versus distance for the 2019 *M* 7.1 Ridgecrest, California, earthquake. We use the high-resolution GAMMA catalog of Lee *et al.* (2020), which uses backprojection methods to detect potential earthquakes, followed by a template-matching algorithm to find additional small earthquakes. For this sequence, the GAMMA catalog has more than 21 times the number of earthquakes reported in the Southern California Seismic Network catalog, with 736,702 earthquakes in total. The GAMMA catalog has 130,571 recorded aftershocks in the first 10 days following the 2019 *M* 7.1 Ridgecrest mainshock; these are the earthquakes we use in our analysis.

We define distance from the mainshock in 2D relative to a line source drawn through dense early aftershocks, as shown in Figure 4. The Ridgecrest mainshock has a far more complicated fault geometry than this, with numerous crosscutting faults, including but not limited to the cross-fault that ruptured in the *M* 6.4 foreshock (Ross, Idini, *et al.*, 2019). We choose not to attempt to closely model the complicated mainshock fault geometry, in part because this could be potentially be overusing the aftershock locations themselves to test a hypothesis about aftershock locations—opening up our analysis to overtuning. Instead we choose a simple line source and hope that any signal will be strong enough to overcome the noise introduced by this simplification. We divide the aftershocks into five quintiles based on their distance in 2D from this line source—from the closest 20% to the farthest 20%.

To show the power of the *a*-positive method, we first estimate aftershock rates conventionally using the raw interevent times in the catalog, with no concern for time-varying event detection. In Figure 5a, we can clearly see that detected earthquake rates are saturated throughout the sequence—approximately constant rates of aftershock detection occur for several of the distance bins, which demonstrates the maximum rate of earthquakes detectable in the GAMMA catalog. For farther distance bins, there is actually an apparent increase in aftershock rate with time from the mainshock. This is due to a combination of (1) the extreme incompleteness immediately following the *M* 7.1 mainshock, which recovers more quickly at larger distances from the mainshock, and (2) Omori decay differences between the distance bins that we better resolve below with improved methods.

In contrast to the raw interevent times, the *a*-positive method can correctly recover Omori decay, even into the mainshock coda, without choosing a minimum magnitude

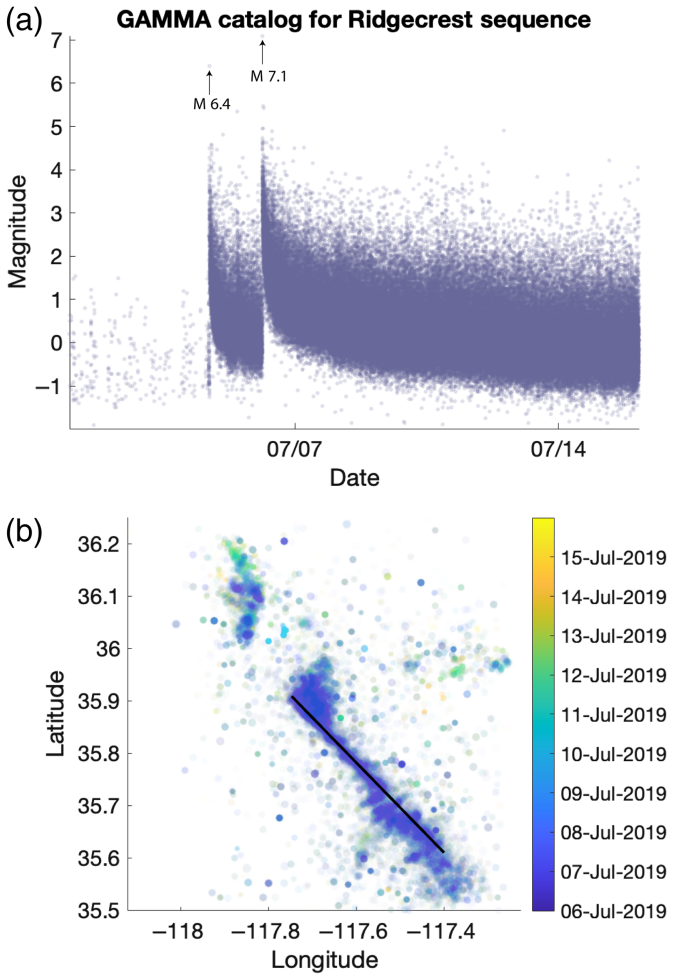

Figure 4. Events in the GAMMA catalog of Lee *et al.* (2020). (a) Magnitude versus time. (b) Locations of the first 10 days of aftershocks following the *M* 7.1 mainshock. The black solid line in panel (b) shows the line source used to define the distance to the mainshock in our analysis. The color version of this figure is available only in the electronic edition.

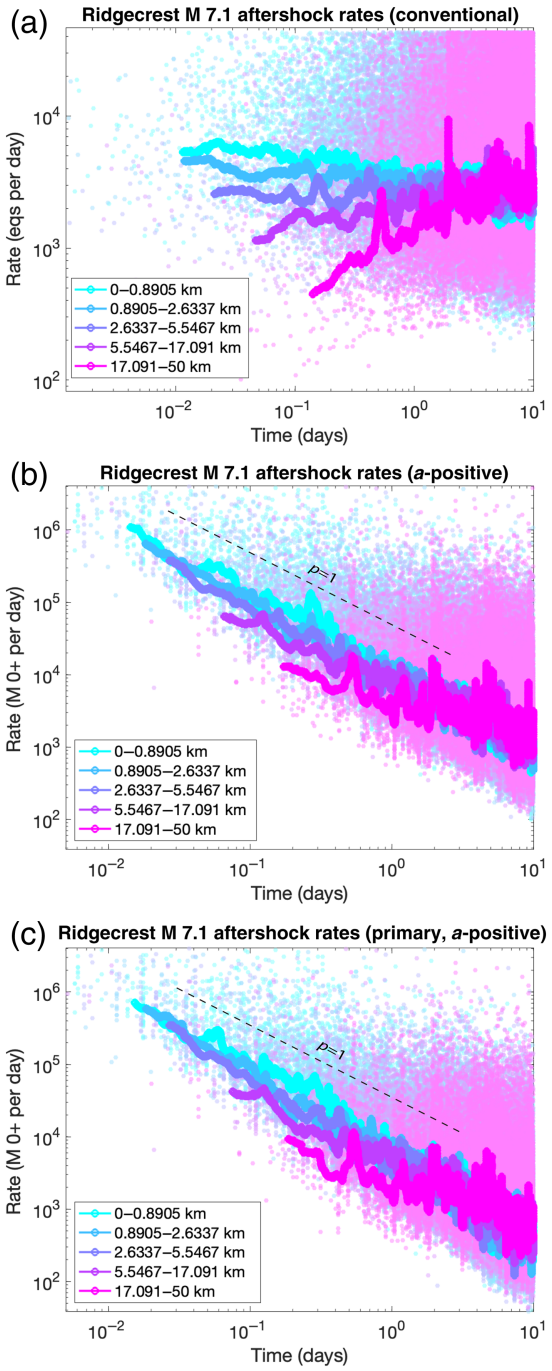

Figure 5. Aftershock rates for the *M* 7.1 Ridgecrest mainshock derived using (a) raw interevent times, (b) the *a*-positive method, and (c) the *a*-positive method, applied to primary aftershocks only, for five bins with equal numbers of detected aftershocks, sorted by distance from the mainshock. All estimates are made using all detected aftershocks within 10 days of the mainshock, without removing events below a minimum magnitude of completeness. The solid lines use 100-event smoothing; raw rate estimates are shown with the transparent circles. The nearest resolvable aftershock rates occur earlier; furthermore, the farthest distance bins resolve some flattening of the aftershock rates at early times consistent with an Omori *c*-value that increases with distance from the mainshock. The color version of this figure is available only in the electronic edition.

of completeness (see Fig. 5b). For these rates (see equation 5), which are scaled to a reference magnitude of M 0, we use a Gutenberg–Richter b-value of 0.82, fit to all aftershocks within the first 10 days of the mainshock using the b-positive method (van der Elst, 2021). We also test using distance-bin-dependent b-value estimates, given that b-values have been observed to vary with distance from the mainshock (Gulia *et al.*, 2018; Sharma *et al.*, 2023), but do not find that this significantly affects our results. Finally, for the results presented here, we use a rather conservative value of $\delta M_c = 0.8$ that works well in our synthetic test. Having tested values of δM_c from 0.4 to 1.2, we do not find that this choice significantly affects our results either.

In Figure 5b, observe that the earliest a-positive aftershock pairs, and thus the first resolvable rates with our method, start later for the farthest distance bins. This is consistent with

equation (4), and can be seen in both the raw rates and in the smoothed rates, which begin at the mean time of the 100th aftershock pair in each bin (the solid lines use 100-event smoothing). For the first three distance quintiles, we do not observe a rolloff in the power-law decay of the aftershock rate with time from the mainshock. For the farthest distance bins, however, we do see evidence of a rolloff in that the curves at early times deviate from $p = 1$ scaling. Both of these observations are consistent with the increase in c-value with distance predicted by rate-and-state friction. They are also consistent with a decrease in the Omori p-value; we do not have sufficient data to distinguish whether the flattening is due to an increase in c or a decrease in p. In any case, as we explain in the Introduction section, lower p-values, in the rate-and-state framework, are due to c-value variability. We would certainly expect some depression of the p-value because our bins necessarily average over a range of stress steps, both because we need enough area to obtain sufficient aftershocks and because of stress heterogeneity.

Note that the flattening of the Omori curves at short times is observed for the most distant bins; these are the bins where we expect the catalog to be most complete. This signal goes against what we would expect to see if these were plateaus due to STAI rather than a real saturation in the aftershock rate. The fact that we do not observe a rate plateau (finite c-value) for the close bins is likely indicative of STAI effects. After all, the a-positive method selects event pairs that are likely complete, but if there are no complete pairs at very early times due to STAI, there will simply be no available rate estimates.

Background rates are quite low for the Ridgecrest dataset relative to aftershock rates (~0.6 $M \geq 2$ earthquakes per day for the region covered by the GAMMA catalog). They are low enough that they are below the axes of the plots in Figure 5 and do not contribute to the flattening of aftershock rates that we observe for the farthest distance bins.

One possibility is that the delay in aftershock occurrence for the farther distance bins is due to secondary triggering since there should be some enlargement of the aftershock zone with time as aftershocks triggered directly by the mainshock go on to trigger their own aftershocks. To investigate this, we use temporal epidemic-type aftershock sequence (ETAS) stochastic declustering (Zhuang *et al.*, 2002) to identify and remove events unlikely to be triggered directly by the mainshock, including aftershocks of foreshocks. One realization of this stochastic declustering, for best-fit maximum-likelihood ETAS parameters, fit to the entire sequence ($p = 1.13$; $c = 0.00392$ days, α fixed to 1.0) is shown in Figure 5c. This shows similar results to the analysis using all aftershocks, although with slightly less scatter because some of the rate fluctuations due to secondary triggering are removed.

In addition to removing the effect of secondary triggering, our declustering attempts to remove aftershocks that are triggered by foreshocks, including the M 6.4 foreshock that occurred ~34 hr before the mainshock. In another test to ensure that the foreshocks are not affecting our results, we repeated the above analysis removing spatial areas with high rates of foreshock activity along the M 6.4 fault plane and the southern part of the M 7.1 fault plane. We find that our results are not significantly affected if these data are removed (see Fig. S2).

We can also consider the effect the M 6.4 foreshock may have on the temporal distribution of the early aftershocks. As mentioned earlier, Dieterich (1994) showed that aftershocks occurring before time c are advanced uniformly by the stress step, preserving their timing relative to each other. The early-time plateau following the mainshock may then show a temporal decay due to the foreshock. How large is this effect? For the most distant spatial bin, we resolve an upper bound on c of about 0.8 days. Over this time interval, the rate from the foreshock changes by only about 30%. This rate change will be challenging to observe in the early aftershock plateau, given the sparseness of the early aftershock data and the fact that the foreshock influences only a small subset of the aftershock zone.

We also present results that are not dependent on smoothing. In Figure 6, we show the cumulative fraction of primary aftershocks occurring with time in the same distance-to-mainshock quintiles, estimated by cumulatively summing the a-positive rates. Here, we can see that the different distance bins have a different underlying rate versus time distribution, irrespective of the total aftershock number. In particular, we see clearly that farther aftershocks occur proportionately later than aftershocks nearer to the M 7.1 Ridgecrest mainshock. This is consistent with the predictions of rate-and-state friction.

The Omori c-value and p-value heavily trade-off on one another in fits and we cannot uniquely constrain each parameter. However, we can assume that the aftershock-rate differences with the distance that we observe are due to c-value variability and check if the fits we obtain with this assumption are consistent with what is predicted by rate-and-state friction. Therefore, we perform a simple calculation to check for consistency with equation (1). For the two farthest bins, where we can see some flattening of the rate at short times relative to the rates in closer bins, we fit an Omori curve, constraining $p = 1$, to the smoothed, declustered a-positive rates. Fits are shown in Figure S3. For the fourth farthest bin, we obtain a c-value estimate of 0.028 ± 0.017 days (error bars give one standard deviation determined from stochastic resamplings of the declustering, which dominates the error). Assuming that the mean static stress step $\Delta\tau$ decays with distance as d^{-3} and $A\sigma$ is constant, equation (1) predicts that

$$\frac{\log(c_4)}{\log(c_5)} = \frac{\Delta\tau_4}{\Delta\tau_5} = \frac{d_5^3}{d_4^3}, \tag{6}$$

with the subscripts denoting bin number. Using the mean distance of aftershocks in bin i for d_i, this predicts that the c-value

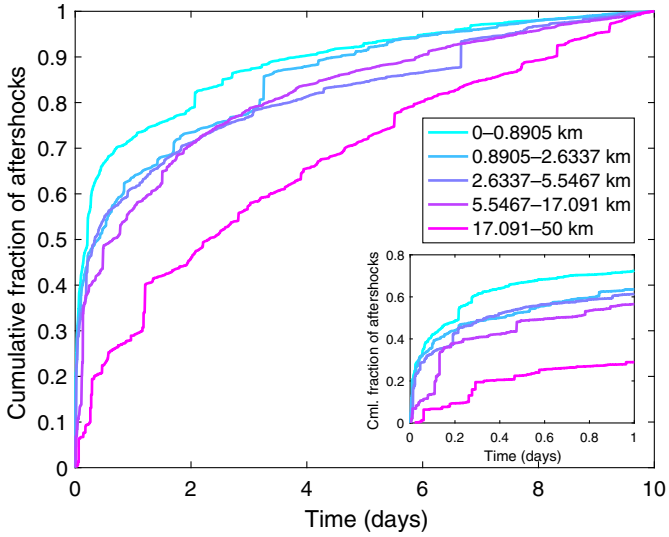

Figure 6. Cumulative fraction of M 7.1 Ridgecrest aftershocks estimated to occur over the first 10 days, calculated using a-positive rates, for quintiles of aftershocks sorted by distance from the mainshock. Far-field aftershocks occur proportionately later in the aftershock sequence than near-field aftershocks. The inset figure shows zoom-in to the first day. The color version of this figure is available only in the electronic edition.

for the fifth farthest should be ~0.79 ± 0.04 days. This agrees remarkably well with our best-fit c-value for the farthest bin of 0.79 ± 0.23 days. Note that this is an approximate calculation because our bins contain a range of stress steps, and therefore under the rate-and-state framework average over a range of c-values (which would look like a lower p-value when fitting a single Omori curve), but it does show that the amount of flattening we observe is consistent with the rate-and-state model.

An additional calculation we perform to check the consistency of our Omori fits with rate-and-state friction is to compare the ratio of our c-value estimates to our estimates of the initial rate R_0 for distance bins 4 and 5. If, in equation (1), we assume that stressing rate $\dot{\tau}_r$ is proportional to background rate r and $A\sigma$ is constant (or follows the same distribution in each bin), this predicts that

$$\frac{R_{0,\mathrm{bin4}}}{R_{0,\mathrm{bin5}}} = \frac{c_5}{c_4}. \tag{7}$$

We find that the ratio of the initial rates agrees within 27% of the ratio of c-values, which is well within a standard deviation of the uncertainty in the fits.

Results for Stacked Aftershock Sequences

We also stack aftershock rates, estimated from the a-positive method, following isolated M 5–6 earthquakes in southern California. We use mainshocks from the QTM catalog (Ross, Trugman, *et al.*, 2019), which uses template matching and includes the period from 2008 to 2017. We use every M 5–6 earthquake not preceded or followed by a larger earthquake within 10 days; these are our mainshocks. With these criteria, we identify 14 mainshocks. Stricter aftershock criteria are required for this analysis, relative to the Ridgecrest sequence, given the higher background rates relative to the aftershock rates. Aftershocks are identified as subsequent earthquakes within 10 km and 1 day of each mainshock. The total number of aftershocks summed over all sequences is 14,246.

Mainshock–aftershock distances are calculated in 3D; we use hypocentral distances unless there are at least seven aftershocks in the first day following the mainshock; in those cases, following van der Elst and Shaw (2015), we define distance relative to the centroid of all first-day aftershocks. This allows better distance measurements to be obtained for mainshock rupture sources that are more unilateral.

We apply the a-positive method to aftershocks for each mainshock individually, and then stack the estimated rates. We use a uniform b-value of 1.0 for all sequences and set δM_c to 0.8. Results are shown in Figure 7. We show the background rate for the farthest distance bin (which has the highest background due to its larger area) with the dashed line. Background rates for the remaining bins are much lower and are off the bottom of the plot.

For the stacked aftershocks of M 5–6 mainshocks, we observe a signal in the same direction as the Ridgecrest results, although it is noisier. On average, the first detected aftershock rates farther from the mainshock start later. Although this appears to suggest a larger Omori c-value for larger-distance bins, it could be due to differences in aftershock number (as with the Ridgecrest analysis, the distance bins are selected so that there is an equal number of detected aftershocks in each bin, which differs from the true number of aftershocks due to incompleteness). For this reason, we also present cumulative results normalized by total aftershock number in Figure 7b. Here we can see that, irrespective of the total number of aftershocks, on average, aftershocks farther from the mainshock occur proportionately later in the sequence than near-field aftershocks. However, this result is noisier than our Ridgecrest results; that is, the curves corresponding to each distance bin are not as well sorted in this plot as with the Ridgecrest analysis.

We are not able to resolve any rolloff due to the c-value for any bin. This is not surprising because there is an order of magnitude less data for this dataset compared to the Ridgecrest dataset. It is also not surprising that the stacked results are noisier than the Ridgecrest results because we are averaging over mainshocks with quite different static stress fields and aftershock productivities. If we are averaging over a wide range of stress steps in each bin, which we would expect to be even more the case for a stack of different mainshocks, we should see flattening of the p-value (Dieterich,

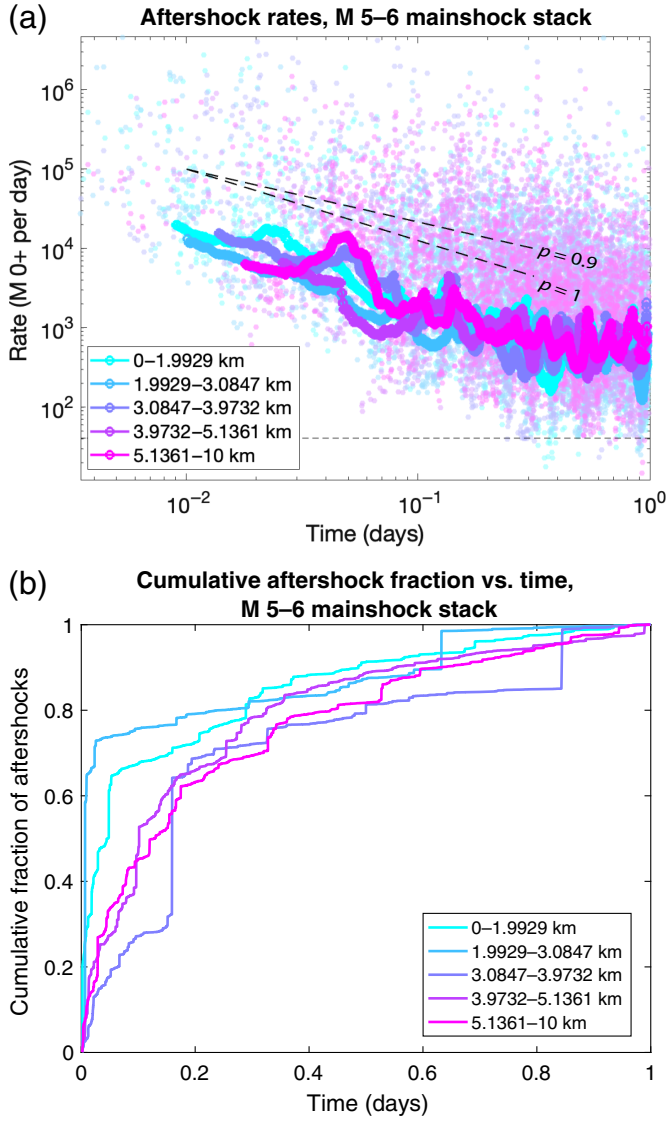

Figure 7. (a) Stacked aftershock rates for different distance bins estimated using the *a*-positive method for isolated *M* 5–6 mainshocks in southern California. The solid lines show 100-event smoothing; raw rate estimates are shown with transparent circles. The background rate for the farthest distance bin is shown with the dotted line. Compare to Figure 5b. (b) Cumulative fraction of aftershocks estimated to occur over the first day, calculated using *a*-positive rates, for quintiles of aftershocks sorted by distance from the mainshock. On average, far-field aftershocks occur proportionately later in the aftershock sequence than near-field aftershocks. Compare to Figure 6. The color version of this figure is available only in the electronic edition.

1994). Indeed, it does appear that *p*-values for the stack are closer to $p = 0.9$ rather than $p = 1$, in contrast to the closest bins for the Ridgecrest data.

Discussion

Together, the Ridgecrest and stacked *M* 5–6 mainshock analyses demonstrate how difficult it is to resolve the true Omori *c*-value; it requires large amounts of aftershocks at large distances and use of the *a*-positive method to recover unsaturated rates to see a flattening of the Omori curve at short times (which, given our resolution, could also be explained with a lower *p*-value). If the rate-and-state model of Dieterich (1994) is correct, the *c*-value is quite small. In the companion article to this one, Hainzl *et al.* (2024) use coseismic stress changes for multiple southern California mainshocks, together with *a*-positive rate calculations that give a maximum bound on the *c*-value, to provide constraints on $A\sigma$ and the background rate spatial decay required to fit the data under the rate-and-state model.

We are able to resolve a reduction in slope at early times consistent with a finite *c*-value for the most distant, lowest-rate aftershock populations following the *M* 7.1 Ridgecrest mainshock, but not for the close-in bins, nor the stacked *M* 5–6 mainshocks in southern California. One of the predictions to come out of the toy slider experiments is that any aftershocks appearing in a plateau prior to time *c* must have been self-nucleating at the time of the mainshock. It is tempting to associate the rolloff in aftershock rate following the Ridgecrest mainshock to earthquakes that were initially stressed by the Ridgecrest foreshock and already accelerating toward failure. The observed absence of the plateau elsewhere could indicate that this is not the condition of aftershock faults, generally.

In this article, we have focused on the predictions of the rate-and-state model of Dieterich (1994), which predicts Omori decay of aftershocks following a static stress step. However, dynamic stresses can also trigger earthquakes (Hill *et al.*, 1993; Felzer and Brodsky, 2006). van der Elst and Brodsky (2010) estimate that 15%–60% of earthquakes are triggered dynamically, based on projections from the far field to the near field. This is consistent with the results of Hardebeck and Harris (2022), who estimate that ~1/3 of aftershocks are dynamically triggered, based on the rates of aftershocks in stress shadows (which while they are depleted relative to regions where the stress has increased, are not observed to have rates below the background rate immediately following the mainshock). Dynamic triggering of some fraction of aftershocks could be another reason why the predicted *c*-value effect of the rate-and-state model is difficult to observe.

The analysis here also assumes a constant $A\sigma$ value for the receiver faults. If $A\sigma$ is not constant but follows some distribution, then for a given stress change and proximity to failure, the sites with the smallest $A\sigma$ will be triggered first (see also the discussion in the companion article by Hainzl *et al.*, 2024 and their Fig. S4). These aftershocks will follow a distribution in time that again exhibits the fundamental $1/t$ scaling, with R_0 and *c* distributed according to equations (2) and (3). Future work may benefit from external constraints on the distribution of $A\sigma$ and fault strength from failure.

Conclusions

We find that for the M 7.1 Ridgecrest mainshock and for stacked M 5–6 mainshocks in California, the farthest aftershocks follow a different decay of rate versus time than the nearest aftershocks. This difference is consistent with the larger c-value predicted by the constitutive friction law of Dieterich (1994) derived from laboratory experiments. Although we can fit the data with many combinations of the Omori parameters p of c, for far aftershocks of the Ridgecrest mainshock, the scaling of the best-fit c-value with distance, when p is constrained to be 1, is consistent with rate-and-state friction and an r^{-3} falloff in stress.

In our analyses, we have used distance to the mainshock as a proxy for stress step. This is advantageous because it is less model dependent than estimating the spatial variability in stress change from a mainshock; however, it is also not the direct quantity we expect to control the Omori c-value. In a companion article to this one, Hainzl *et al.* (2024) derives stress change models from multiple finite-source rupture models for the six largest recent mainshocks in southern California. Their results are consistent with ours in that c-values are required to be very small; bounds on c are used to put a maximum bound on $A\sigma$ in equation (1).

Early aftershock rates are difficult to resolve; we can only resolve a flattening of the Omori curve for the farthest aftershocks for an incredibly high-resolution catalog for the Ridgecrest mainshock with ∼130,000 detected events. As more high-resolution catalogs become available for large earthquakes, however, additional tests of the rate-and-state prediction for c-value could be made. Furthermore, the onset of the earliest aftershocks, if they can be resolved, could constrain the proximity to failure for faults on which aftershocks occur.

Data and Resources

The GAMMA catalog of Lee *et al.* (2020) is available at http://bit.ly/2WswZQk (last accessed July 2023). The QTM catalog (Ross, Trugman, *et al.*, 2019) is available at https://scedc.caltech.edu/eq-catalogs/altcatalogs.html (last accessed August 2020). The supplemental material includes three additional figures: additional results from numerical modeling of the frictional slider, a reanalysis of the Ridgecrest aftershock results with active foreshock zones excluded, and constrained Omori fits for each of the distance bins in the Ridgecrest dataset.

Declaration of Competing Interests

The authors acknowledge that there are no conflicts of interest recorded.

Acknowledgments

The authors thank Karen Felzer for many comments that helped make our analysis more robust. The authors also thank Andrea Llenos, three anonymous reviewers, and the associate editor for their constructive reviews. Any use of trade, firm, or product names is for descriptive purposes only and does not imply endorsement by the U.S. Government.

References

Beeler, N. M., and D. A. Lockner (2003). Why earthquakes correlate weakly with the solid earth tides: Effects of periodic stress on the rate and probability of earthquake occurrence, *J. Geophys. Res.* **108,** no. B8, 2391, doi: 10.1029/2001JB001518.

Bhattacharya, P., A. M. Rubin, and N. M. Beeler (2017). Does fault strengthening in laboratory rock friction experiments really depend primarily upon time and not slip? *J. Geophys. Res.* **122,** no. 8, 6389–6430.

Dieterich, J. A. (1992). Earthquake nucleation on faults with rate and state-dependent friction, *Tectonophysics* **211,** 149–178.

Dieterich, J. A. (1994). Constitutive law for the rate of earthquake production and its application to earthquake clustering, *J. Geophys. Res.* **99,** 2601–2618.

Felzer, K. R., and E. E. Brodsky (2006). Decay of aftershock density with distance indicates triggering by dynamic stress, *Nature* **441,** 735–738.

Gomberg, J., N. Beeler, and M. Blanpied (2000). On rate-state and Coulomb failure models, *J. Geophys. Res.* **105,** no. 4, 7857–7871.

Gulia, L., A. P. Rinaldi, T. Tormann, G. Vannucci, B. Enescu, and S. Wiemer (2018). The effect of a mainshock on the size distribution of the aftershocks, *Geophys. Res. Lett.* **45,** no. 24, 13,277–13,287.

Gutenberg, B., and C. F. Richter (1944). Frequency of earthquakes in California, *Bull. Seismol. Soc. Am.* **4,** 185–188.

Hainzl, S., M. T. Page, and N. van der Elst (2024). Onset of aftershocks: Constraints on the rate-and-state model, *Seismol. Res. Lett.* doi: 10.1785/0220240176.

Hardebeck, J. L., and R. A. Harris (2022). Earthquakes in the shadows: Why aftershocks occur at surprising locations, *Seism. Rec.* **2,** no. 3, 207–216.

Harris, R. A., and R. W. Simpson (1998). Suppression of large earthquakes by stress shadows: A comparison of Coulomb and rate-and-state failure, *J. Geophys. Res.* **103,** 24,439–24,451.

Heimisson, E. R., and P. Segall (2018). Constitutive law for earthquake production based on rate-and-state friction: Dieterich 1994 revisited, *J. Geophys. Res.* **123,** no. 5, 4141–4156.

Helmstetter, A., Y. Y. Kagan, and D. D. Jackson (2006). Comparison of short-term and time-independent earthquake forecast models for southern California, *Bull. Seismol. Soc. Am.* **96,** 90–106.

Herrmann, M., and W. Marzocchi (2020). Inconsistencies and lurking pitfalls in the magnitude-frequency distribution of high-resolution earthquake catalogs, *Seismol. Res. Lett.* **92,** no. 2A, 909–922.

Hill, D. P., P. A. Reasenberg, A. Michael, W. J. Arabaz, G. Beroza, D. Brumbaugh, J. N. Brune, R. Castro, S. Davis, D. dePolo, *et al.* (1993). Seismicity remotely triggered by the magnitude 7.3 Landers, California, earthquake, *Science* **260,** 1617–1623.

Kagan, Y. Y. (2004). Short-term properties of earthquake catalogs and models of earthquake source, *Bull. Seismol. Soc. Am.* **94,** 1207–1228.

Kagan, Y. Y., and H. Houston (2005). Relation between mainshock rupture process and Omori's law for aftershock moment release rate, *Geophys. J. Int.* **163,** no. 3, 1039–1048.

Lee, E., W. Liao, D. Mu, W. Wang, and P. Chen (2020). GPU-accelerated automatic microseismic monitoring algorithm (GAMMA) and its application to the 2019 Ridgecrest earthquake sequence, *Seismol. Res. Lett.* **91,** no. 4, 2062–2074.

Mallman, E. P., and T. Parsons (2008). A global search for stress shadows, *J. Geophys. Res.* **113,** no. B12, doi: 10.1029/2007JB005336.

Omori, F. (1895). On after-shocks of earthquakes, *J. Coll. Sci. Imp. Univ. Tokyo* **7,** no. 2, 111–200.

Page, M. T., and N. J. van der Elst (2022). Aftershocks preferentially occur in previously active areas, *Seism. Rec.* **2,** no. 2, 100–106.

Rice, J. R., and A. L. Ruina (1983). Stability of steady frictional slipping, *J. Appl. Mech.* **50,** no. 2, 343–349.

Ringdal, F. (1976). Maximum-likelihood estimation of seismic magnitude, *Bull. Seismol. Soc. Am.* **66,** 789–802.

Ross, Z. E., B. Idini, Z. Jia, O. L. Stephenson, M. Zhong, X. Wang, Z. Zhan, M. Simons, E. J. Fielding, S.-H. Yun, *et al.* (2019). Hierarchical interlocked orthogonal faulting in the 2019 Ridgecrest earthquake sequence, *Science* **366,** no. 6463, 346–351.

Ross, Z. E., D. T. Trugman, E. Hauksson, and P. M. Shearer (2019). Searching for hidden earthquakes in Southern California, *Science* **364,** no. 6442, 767–771.

Sharma, S., S. Hainzl, and G. Zoller (2023). Seismicity parameters dependence on main shock-induced co-seismic stress, *Geophys. J. Int.* **235,** no. 1, 509–517.

Utsu, T. (1961). A statistical study on the occurrence of aftershocks, *Geophys. Mag.* **30,** 521–605.

van der Elst, N. J. (2021). *b*-positive: A robust estimator of aftershock magnitude distribution in transiently incomplete catalogs, *J. Geophys. Res.* **126,** no. 2, e2020JB021027, doi: 10.1029/2020JB021027.

van der Elst, N. J., and E. E. Brodsky (2010). Connecting near-field and far-field earthquake triggering to dynamic strain, *J. Geophys. Res.* **115,** no. B7, doi: 10.1029/2009JB006681.

van der Elst, N. J., and M. T. Page (2023). *a*-positive: A robust estimator of the earthquake rate in incomplete or saturated catalogs, *J. Geophys. Res.* **128,** no. 10, e2023JB027089, doi: 10.1029/2023JB027089.

van der Elst, N. J., and H. M. Savage (2015). Frequency dependence of delayed and instantaneous triggering on laboratory and simulated faults governed by rate-state friction, *J. Geophys. Res.* **120,** no. 5, 3406–3429.

van der Elst, N. J., and B. E. Shaw (2015). Larger aftershocks happen farther away: Nonseparability of magnitude and spatial distributions of aftershocks, *Geophys. Res. Lett.* **42,** no. 14, 5771–5778.

Zhuang, J., Y. Ogata, and D. Vere-Jones (2002). Stochastic declustering of space-time earthquake occurrences, *J. Am. Stat. Assoc.* **97,** no. 458, 369–380.

Manuscript received 6 May 2024
Published online 23 September 2024